Doping nature of group V elements in ZnO single crystals grown from melts at high pressure

Nikolai Taibarei, Vladimir Kytin, Elizaveta Konstantinova, Vladimir Kulbachinskii, Olga Shalygina, Alexander Pavlikov, Serguei Savilov, Viktor Tafeenko, Vladimir Mukhanov, Vladimir Solozhenko, et al.

Doping nature of group V elements in ZnO single crystals grown from melts at high pressure

Nikolai O. Taibarei[1], Vladimir G. Kytin[2], Elizaveta A. Konstantinova[2], Vladimir A. Kulbachinskii[2], Olga A. Shalygina[2], Alexander V. Pavlikov[2], Serguei V. Savilov[1], Viktor A. Tafeenko[1], Vladimir A. Mukhanov[3], Vladimir L. Solozhenko[3], Andrei N. Baranov*[1]

[1] *Department of Chemistry, Lomonosov Moscow State University, 119991, Moscow, Russia*

[2] *Department of Physics, Lomonosov Moscow State University, 119991, Moscow, Russia*

[3] *LSPM–CNRS, Université Sorbonne Paris Nord, 93430 Villetaneuse, France*

Abstract

ZnO single crystals doped with group-V elements have been grown from melt at high pressure. Dopants were introduced in several forms such as Sb_2O_3, P, As, Sb and Zn_3X_2 (X = P, As, Sb) in the high-pressure cell. Systematic studies of morphology were performed using optical microscopy and scanning electron microscopy. Crystal structure and lattice parameters were studied using X-ray diffraction and X-ray crystallography. Crystals exhibited distinct changes of size, shape and color compared to undoped ZnO melt-grown single crystals due to the dopants influence. X-ray photoelectron spectroscopy was used to determine valence states of group-V elements when incorporated in ZnO lattice. Photoluminescence, Raman spectroscopy and electron paramagnetic resonance spectroscopy were employed to investigate the nature of defects formed as the result of doping. Formation of V_{Zn} and V_{Zn}-complexes was confirmed and their concentrations were measured. Estimates of the number of V_{Zn} per one dopant atom showed that the ratio is noticeably higher than the one suggested for the shallow complex $As(P, Sb)_{Zn}$-$2V_{Zn}$ commonly regarded as responsible for acceptor properties in ZnO.

1 Introduction

ZnO is a II-VI n-type direct wide band gap semiconductor with and gap of 3.37 eV and large exciton binding energy of 60 meV at room temperature[1-3]. Such combination of physical properties makes ZnO an attractive material for various electronic applications such as ultraviolet light-emitting diodes and laser diodes with low thresholds[4-5]. These semiconductor devices demand a stable p-n homojunction, which consequently requires creation of p-type conductivity in ZnO.

* email address for correspondence: anb@inorg.chem.msu.ru

ZnO semiconductor properties are considered to be provided by certain native point defects (oxygen vacancies (V_O) and interstitial zinc (Zn_i)[6-7] or hydrogen impurities[8] according to the common accepted point of view. However, the fabrication of stable and reproducible p-type ZnO has been difficult due to the self-compensation, the low solubility of the acceptor dopants (typically $<10^{18}$ cm^{-3}) and large ionization energy (170–380 meV) of all probable acceptor dopants[9-12]. Among potential dopants for p-type doping of ZnO, the elements of group V (P, As, Sb) drew attention following the idea of doping with large-size-mismatched impurities leading to formation of the shallow acceptor complex $Sb(P, As)_{Zn}$-$2V_{Zn}$[13]. Such complexes contain the doping atom in the +5 oxidation state substituting cation in contrast to previously considered substitution of anion in -3 oxidation state[14-15]. Recently, there have been a number of reports on obtaining of p-type ZnO through doping with P[16], As[17] and Sb[18-19]. In those works, samples of ZnO were formed as different types of nanostructures: thin films, nanorods and nanobelts.

While the absolute majority of works deal with physical techniques of thin film growth, a considerably smaller amount of papers describes doping of ZnO single crystal. Since performance of thin films is strongly dependent on their quality, which also tends to degrade with the introduction of dopants, a semiconductor single crystal would be a desirable object for investigation of electrical properties of the material. However, there are certain difficulties with obtaining single crystal of ZnO doped with group-V elements. Four methods are known for ZnO single crystal growth: hydrothermal, growth from the melt, vapor transport, and flux growth[20] among which hydrothermal growth is the most commonly applied. Incorporation of a dopant, which is essentially an impurity, poses additional obstacles to growth of quality single crystal. Thus, doping with group-V elements during hydrothermal growth is difficult as there are almost no compounds stable at the growth conditions containing those elements in a cation form while incorporation in an anion form is unlikely due to a strong competition with OH^- ions in a basic medium. Another problem is incorporation of self-compensating hydrogen impurities during hydrothermal growth.

Previous attempts of doping ZnO with Sb using hydrothermal approach did not result in p-type conductivity[21]. The purity of crystals grown by vapor transport is superior in comparison with hydrothermal method. However, it is difficult to synthesize doped crystals because impurities impede the growth process in that case. Moreover, accessibility of dopant source might be an additional challenge. Instead of growing doped ZnO single crystals, there were attempts of introducing P[22] and Sb[23] via annealing of prepared single crystals in the vapor. An alternative approach of introducing dopant by ion implantation was realized for As[24]. The problems of the flux method are similar to the hydrothermal method and deal with incorporation of impurities from the flux[25]. The growth of bulk ZnO crystal from the melt could be preferential compared to other options but is complicated by the fact that the triple point of ZnO is 2248(25) K and 1.06 bar. Consequently, in order to maintain ZnO melt, it requires pressures of 50-100 bar, because at the melting point the substance evaporates with dissociation[26].

Previously, a technique of ZnO crystal growth by spontaneous crystallization from the melt at pressure of 4.2 GPa and temperature of 1800 K in a large-volume high-pressure apparatus was

developed[27]. Such an approach allows avoiding the problem of excessively high temperatures in the melt method while preserving its advantage of adding any desired impurity. Here we extend this technique for systems where various dopant sources containing group-V elements were added in the high-pressure cell along with ZnO. The method yields high quality single crystals suitable for studying fundamental properties of the material.

2 Experimental

The crystal growth was carried out at LSPM–CNRS in a specially designed high-temperature cell of a toroid-type high-pressure apparatus equipped with direct-current heating system. Details of pressure and temperature calibration have been described earlier[28-29]. The high-pressure cell was filled with ZnO microcrystalline powder (325 mesh, 99.9995% Alfa Aesar) mixed with one of the following dopants: Sb_2O_3 (99.999%, Sigma-Aldrich); Sb (99,999%, Sigma-Aldrich); Zn (99.999%, Sigma-Aldrich) + Sb; As (99,999%, Sigma-Aldrich); Zn + As; P (99.999%, Sigma-Aldrich); Zn + P. Zn + X dopants were taken in 3:2 atomic ratio as for Zn_3X_2 stoichiometric compounds to introduce the group-V elements in X^{-3} state. The powders were thoroughly grinded and then pressurized into a disk of 3.5 mm in diameter and 3 mm in height that was then gradually compressed up to 4.0 GPa and heated to 1700–1900 K with an average heating rate of 500 K/min. After holding for 1–2 min at the given temperature the high-pressure cell was rapidly (~300 K/s) quenched by switching off the electric power and then slowly decompressed. It is important to mention that no observable difference in the morphology and composition was found between quenched and slowly cooled samples. Therefore, in all experiments samples were rapidly quenched as it significantly shortens the duration of the experiment.

Samples were recovered in the form of sintered discs, which were later destructed into individual crystals. The morphology of doped crystals was studied by optical microscopy on an Eclipse 600pol (Nikon) and scanning electron microscopy (SEM) on a Supra 50 VP (LEO) equipped with INCA Energy 450 Xmax 80 (Oxford Instruments) microanalysis system. X-ray diffraction (XRD) patterns were collected using Rigaku D/MAX-2500V/PC X-ray diffractometer with rotation anode (CuKα1 radiation (λ = 0.15418 nm), scan step size of 0.02°).

Undoped ZnO crystals grown from the melt are known to form lightly colored and nearly transparent nanorods of hexagonal shape due to a higher growth rate along the *c*-axis[30]. Crystals of ZnO doped in low (1-2 %) concentrations grow without a preferential growth orientation and with a relatively uniform size distribution often with deformed hexagonal facets and colors ranging from yellow-orange for the samples doped with Sb to black for the As-doped samples (Fig. 1a). As concentration of a dopant increases, samples demonstrate a tendency to form a blend of rod-like crystals very similar to undoped ZnO (but of a much smaller size) and colored deformed aggregates of crystals attributing to doped ZnO (Fig 1b). Addition of an impurity expectedly impedes crystal growth and leads to formation of smaller crystals.

Moreover, impurities may slow down normally accelerated growth along the *c*-axis causing crystals to have a shape with no preferential direction. A visible change of shape and color combined with no Sb-associated peaks on XRD patterns implies successful incorporation of the dopant in ZnO structure. Sometimes the resulting samples might represent a blend of orange spherical and dark rod-like particles (Fig. 1b), which indicates a non-uniform distribution of the dopant. This effect usually holds for higher concentrations of Sb (2-5%).

Doping with P-based and Zn + X dopants often leads to formation of smaller (10-20 μm) crystallites with no apparent shape and abundant inclusions on the surface (Fig. 2b). Optically such samples look like particles with rough surface, and sometimes the color might differ within one particle suggesting polycrystalline nature of the latter. Given that there were no reproducibly obtained phosphorus-doped single crystals, P-doped samples were partly excluded from further studying.

The size of crystals estimated from SEM and optical microscopy images varies for different compositions not exceeding 400 μm but is generally below 100 μm. That, in contrast to undoped crystals often reaching 1 mm in length, is expected since in the presence of an impurity the nucleation rate increases over the growth rate. Such effect is particularly noticeable for P-doped samples due to intense chemical interaction between ZnO melt and phosphorus:

$$8\mathrm{ZnO} + 2\mathrm{P} \rightarrow \mathrm{Zn_3(PO_4)_2} + 5\mathrm{Zn} \qquad (1)$$

that produces phosphate-anions capable of incorporation onto positively charged Zn-face surface of growing crystals leading to termination of the growth and formation of a polycrystalline product. Similar reactions are not possible for As and Sb due to the increase of metallic properties in the P-As-Sb group.

In the case of low (1 mol%) concentration of dopants the synthesis yields pure ZnO phase with no detectable impurities with the exception of metallic Sb where a small amount of Sb is observed in XRD and EDX. In the case of P-doping XRD patterns (Fig.3a) reveal the presence of $Zn_3(PO_4)_2$, which proves that reaction (1) indeed takes place in the high-pressure cell. Doping with Zn_3Sb_2 interestingly leads to formation of ZnSb phase [ICDD 5-714] that can be observed in XRD patterns (Fig.3b). The change in atomic ratio between Zn and Sb compared to Zn_3Sb_2 implies that zinc partially incorporates in the ZnO structure. Effects of Zn-doping can be particularly seen in photoluminescence of such samples as discussed later. Additionally, powder XRD patterns may contain lines from dopant-unrelated impurities – primarily carbon and silicates from the material of the high-pressure cell. However, these impurities can be removed mechanically during crystal selection. Overall, information about the samples with the respective names, composition and results of powder XRD and morphology analysis is summarized in Table 1. The best results in regard of single crystal size were achieved by doping with elemental Sb and As reaching 200 μm in diameter. These crystals were also used to study dopant concentrations by EDX measurements. The average concentration in at least 10 crystals was found to be ~0.3 at% for both As and Sb.

The parameters of unit cells of 7 single ocrystals of zinc oxide doped with antimony (I), two single crystals of pure zinc oxide (II) and 1 crystal – zinc oxide doped with arsenic (III), have been determined.

The diffraction data of ZnO:Sb, ZnO, ZnO:As were collected by using STOE diffractometer (Pilatus 100K detector, focusing mirror collimation, CuKα (1.54086 Å) radiation) in rotation method mode. STOE X-AREA software was used for cell refinement and data reduction. Data collection and image processing was performed with X-Area 1.67 software (STOE & Cie GmbH, Darmstadt, Germany, 2013). Intensity data were scaled with LANA (part of X-Area) in order to minimize differences of intensities of symmetry-equivalent reflections (multi-scan method).

Unit cell parameters (I) are in the range a = 3.248–3.249(1) Å, c = 5.195–5.209(1) Å; (II) a = 3.243, 3.246(1) Å; c= 5.209, 5.197 (1) Å; (III) a = 3.2454(2) Å; c = 5.1987(4) Å. Parameters remain the same for different initial concentrations of Sb. It is in agreement with the EDX results where concentrations were found to be ~0.3 at%. The average values of the unit cell volumes are 47.55(2), 47.43(2) and 47.42(2) $Å^3$ for (I), (II) and (III), respectively.

Antimony-doped single crystals are of good quality and have a unit cell volume of 0.13 $Å^3$ higher than pure zinc oxide. This is in agreement with the ionic radius difference between Sb^{3+} (0.76 Å) and Zn^{2+} (0.6 Å). Ionic radius of As^{3+} (0.58 Å) is very close to that of Zn^{2+}, consequently, there is no noticeable difference in unit cell volume.

3 Results and discussion

3.1 . X-ray photoelectron spectroscopy

The oxidation states of the dopant elements were studied by X-ray photoelectron spectroscopy (XPS) on a Kratos AXIS Ultra DLD spectrometer. Deconvolution of the spectra was performed in CasaXPS program package. There were two series of experiments: in the first one as-recovered discs were used, in the second one Ar^+-beam etching was applied in order to study deeper layers of the material. The spectra from the surface of the samples are shown in Fig. 4.

For ZSb01_1 and ZSb01_3, it was derived from the Sb3d3/2 peaks (Fig. 4a) that Sb has both Sb^{+3} and Sb^{+5} oxidation states in the case of when Sb_2O_3 and Sb were used as dopant sources. In ZSb05_2 only the Sb^{+3} component was observed and its intensity is substantially lower than for other samples. As shown by XRD, most of Sb is bound in ZnSb intermetallic with a much lower crystallization temperature than ZnO, which might lead to significant inhomogeneity of Sb distribution in the sample. In the sample doped with Sb, the intensities of Sb^{+3} and Sb^{+5} components are close in comparison with the case of Sb_2O_3 doping where the Sb^{+3} component is dominating.

The oxidation state of the dopant in samples doped with As and Zn_3As_2 determined from As3d peak was always found to be a mix of As^{+3} and As^{+5} oxidation states (Fig. 4b). While it is likely that As naturally forms (III) and (V) centers under synthesis conditions, it might also be due to reduction of As by electron beam during XPS measurements[31].

P2p peaks of phosphorus in samples doped with P and Zn_3P_2 always fall in the range from 133.2 to 134.3 eV (Fig. 4c) that corresponds to compounds containing P^{+5} oxidation state. While it is hard to predict the exact coordination of phosphorus in the samples, small shifts in peak position suggest that different forms of initial dopants might produce different types of P-based centers. In addition, there is a difference in phosphorus content determined by EDX between P- and Zn_3P_2-doped samples, similar to doping with Sb and Zn_3Sb_2, with a much lower phosphorus concentration in the latter (about 2.0 % for P-doped and 0.8 % for Zn_3P_2-doped samples) found by EDX.

In the previous study[23] we showed that doping of ZnO single crystals by Sb from the vapor in the absence of an external oxidant results in the ZnO structure containing exclusively Sb^{+5} when only surface layers are studied. One would assume that a different situation might hold for the bulk of doped ZnO. XPS spectra recorded with Ar^+ etching support this idea revealing the presence of Sb^{+3} and Sb^0 in deeper layers of Sb_2O_3-doped samples and no Sb^{+5} component (Fig. 5a).

Sb^0 – the product of reduction of Sb_2O_3 by carbon of the graphite heater – is, in fact, responsible for the appearance of Sb^{+5} states in the surface layers. In[32], it was demonstrated that atmospheric oxygen gradually oxidizes metallic Sb, which results in Sb^{+5} signal in XPS spectra. Note, that the Sb^{+5}/Sb^{+3} intensity ratio is higher for ZSb01_3 in the initial spectrum than for ZSb01_1 (Fig. 4a) due to the availability of excess metallic Sb while in the case of ZSb01_1 the only source of Sb^0 is a relatively small amount of reduced antimony, which is below detection limit of XRD. Therefore, Sb^{+5} states are created via atmospheric oxidation of metallic Sb while Sb^{+3} states stabilized both in ZnO lattice and in excess Sb_2O_3 are not susceptible to such oxidation. Interestingly, the binding energy of Sb(III) component of the Sb3d3/2 peak on the surface is 539.5 eV, which precisely corresponds to Sb_2O_3 while after Ar^+ etching this energy increases to 539.7 eV (Fig. 5a). This observation indirectly proves incorporation of Sb in ZnO lattice where it forms impurity centers with oxygen coordination differing from its native oxide.

The spectrum of Zn_3As_2-doped sample (Fig. 5b) demonstrates significantly increased As^{+3}/As^{+5} intensity ratio after Ar^+ etching along with the appearance of As^0 component that becomes exposed after the removal of the oxidized layer via etching, similarly to the Sb_2O_3-doped sample, though low intensity As^{+5} component can still be observed in this case. However, the P-doped sample contains only a P^{+5} signal (Fig. 5c) since it is the most stable oxidation state of phosphorus.

3.2 *Photoluminescence and Raman spectroscopy*

Photoluminescence (PL) spectra of the samples were measured at room temperature in air using a SOLAR TII MS 35041 grating monochromator equipped with a Hamamatsu CCD detector. The PL excitation was done by He-Cd laser (325 nm).

A typical PL spectrum of ZnO single crystals doped with group-V elements or their oxides is shown in Fig. 6. The spectrum contains a very broad band of defect-associated luminescence that extends from about 400 nm to about 800 nm. The band has a discernible “shoulder” in the high-energy range, an absolute maximum around 600 nm and a long “tail” in the low-energy range. While the procedure of Gaussian deconvolution of PL bands is not always correct due to asymmetric nature of

individual bands[33], in our case it is justified since the band is clearly composed of at least three bands of substantially different origin.

Such a spectrum can be deconvoluted into three bands that can be assigned to so-called green luminescence (GL), yellow luminescence (YL) and red luminescence (RL) of ZnO. The slightly asymmetric GL band with the maximum around 490 nm (2.53 eV) and FWHM = 0.53 eV is very characteristic for ZnO and was observed many times in various ZnO-related materials[34]. This luminescence is commonly assigned to intrinsic donor-type point defects such as V_O. The band of YL with a maximum around 565 nm (2.19 eV) was previously observed in melt-grown samples of ZnO[35] and ascribed to deep V_{Zn}-related acceptors with the activation energy of ~0.4 eV. The shape of RL band varies from sample to sample but its maximum remains between 630 and 640 nm. Nature of red luminescence is less studied in the literature, according to[36] it is probably due to defect complexes V_O-Zn_i and $V_{Zn}V_O$ – both seem to be possible given the availability of excess Zn, which could be included in interstices and the presence of V_{Zn} suggested by both photoluminescence and EPR as described later. Additionally, there was no significant difference found in luminescence spectra recorded from only one single crystal and a collective of randomly selected crystals. The respective intensities of the bands and their maxima positions change slightly suggesting a certain level of inhomogeneity but the shape of the line remains similar. Doped ZnO single crystals generally exhibit a very high intensity of photoluminescence. Near band edge (NBE) luminescence can be observed at room temperature (Fig. 6, inset). The peak at 380 nm corresponds to the recombination of excitons; the peak at 393 nm can be attributed to the recombination of donor-acceptor pairs[37-38]. This confirms formation of acceptor centers in doped samples.

In contrast, when doped with Zn_3X_2-type dopants the luminescence spectra change dramatically and exhibit only a single symmetrical violet-blue peak (Fig. 7) with the maximum between 410 and 430 nm depending on the sample. Such luminescence in ZnO was previously attributed to Zn_i defects[39] that are formed in the presence of large quantities of Zn and seem to be the only type of defect presented in such samples. Moreover, the shape of the spectra is close to the one recorded for undoped ZnO melt-grown single crystals[27] though the peak maximum is shifted in the blue region. The intensity of such luminescence is much lower and other types of luminescence are almost entirely extinguished.

Backscattered Raman spectra were measured using a Horiba HR800 micro-Raman spectrometer at room temperature. Linearly polarized laser radiation with a wavelength of 488 nm was used for excitation. Typical Raman spectra are presented in Fig. 8. Peaks corresponding to single-phonon modes (A_1(TO) at 380 cm^{-1}, E_1(TO) at 408 cm^{-1}, E_2^{high} at 437 cm^{-1}) are clearly visible in the spectra[40].

Measurements carried out in polarized light (see Fig.9) showed that the intensity of these modes changes depending on the orientation of the analyzer. This dependence indicates that the samples under study are single crystals.

The A_1(TO) phonon peaks are shifted by about 2.4 cm^{-1} towards lower wavenumbers for the sample doped with As (ZAs02_3) and Sb (ZSb01_3) as compared to the undoped one (inset in Fig. 8). It is known that in A_1(TO) Zn and O atoms move in opposite directions along the *C3* axis[41].

Following expression is presented in[42] for this type of transversal optical phonons in long wavelength (phonon wavelength much longer than interatomic distance) continuum limit:

$$\omega_{A_1} = \frac{q\sqrt{N}(\varepsilon_\infty+2)}{3\sqrt{\varepsilon_0\mu(\varepsilon-\varepsilon_\infty)}} \quad (2)$$

where q is the charge of ion; ε_0 is the electric constant, $N = \frac{N_+ + N_-}{2}$ is the mean concentration of positive and negative ions contributing to phonon mode with concentrations N_+ and N_-, correspondingly; $\mu = \frac{M_+ M_-}{M_+ + M_-}$ is the reduced effective mass of positive and negative ions contributing to phonon mode with masses M_+ and M_-, correspondingly; ε and ε_∞ are the static and high frequency dielectric permittivity. Note, that expression (2) gives reasonable estimate for A_1(TO) peak position k_0=358 cm^{-1} in ZnO. For this estimate we took Millikan charge calculated for ZnO clusters q=0.9e (e is the elementary charge)[43], $\varepsilon_\infty = n_0^2$=4 ($n_0$ is the refractive index)[44], ε=8.6[45]. This shows applicability of the simplified expression (2) for A_1(TO) mode. Suppose that dielectric permittivity is independent on ion concentration in static and high frequency limit. Then following relative shift of phonon frequency $\frac{\Delta\omega_{A_1}}{\omega_{A_1}}$ and Raman peak position $\frac{\Delta k_{A_1}}{k_{A_1}}$ is expected for small variation of positive ion concentration $\frac{\Delta N_+}{N}$.

$$\frac{\Delta\omega_{A_1}}{\omega_{A_1}} = \frac{\Delta k_{A_1}}{k_{A_1}} = \frac{1}{4}\frac{\Delta N_+}{N} \quad (3)$$

where Δk_{A_1} is the shift of Raman peak position caused by variation of positive ion concentration, Δk_{A_1} is the initial Raman peak position. Doping of ZnO with Sb and As leads to substitution of one Zn atom by Sb or As and possible creation of n_V Zn vacancies per one As or Sb atom. Thus doping of ZnO with Sb and As should lead to reduction of concentration of Zn ions and frequency of A_1(TO) phonon. For Sb or As content per one Zn atom equal to *c* relative shift of A_1(TO) Raman peak can be estimated as:

$$\frac{\Delta k_{A_1}}{k_{A_1}} = \frac{-1}{4}(n_V + 1)c \quad (4)$$

For As in ZAs02_3 and Sb in ZSb01_3 samples c=0.003-0.005. For n_V=2 this gives estimate of the shift of Raman peak $\Delta k_{A_1} = (0.9 - 1.4)\ cm^{-1}$. This estimate is in qualitative agreement with experiment but smaller than observed difference in Raman shifts of the A_1(TO) mode in samples doped with As and Sb compared to the undoped sample. (inset in Fig. 8). Better agreement corresponds to n_V=3.4-5.3. Thus, the Raman spectroscopy data are consistent with the creation of two Zn vacancies by Sb or As substitution. Substitution of Zn by Sb or As and creation of Zn vacancies should produce local vibration modes. Such effect was observed in[46]. We suppose that the intensity of such modes in our samples is at least 200 times smaller (ratio of Sb or As atom

concentration to Zn atom concentration) than intensity of ZnO peaks. This is below the sensitivity of our Raman spectrometer.

3.3. EPR spectroscopy

Electron paramagnetic resonance spectra have been recorded with an ELEXSYS-E500 (Bruker, Germany) spectrometer (X-band, the sensitivity up to 10^{10} spin/g) at stabilized temperature. The measurement temperature was kept at 130-300 K range with a Bruker ER 4112HV temperature control system. The concentration of paramagnetic centers (PCs) was evaluated using $CuCl_2 \cdot 2H_2O$ single crystal with known number of spins as the standard. Recorded EPR spectra are shown in Fig. 8. Estimates of PCs are listed in Table 2.

For visual separation spectra are shifted in vertical direction. Spectra were normalized to the samples masses. For undoped ZnO sample only asymmetric signal with g-factor close to 1.955 has been observed. The ratio of positive peak to negative one is equal to 2.0 at 130 K and 2.3 at 180 K. An estimate of these paramagnetic defects is equal to $5.5 \cdot 10^{19}$ spin/g at 130 K and $4.6 \cdot 10^{19}$ spin/g at 180 K.

Asymmetry of the signal could originate from skin effect due to relatively high electrical conductivity of the sample[47]. In particular, skin penetration depth calculated for static electrical resistivity is about 50 μm, which is smaller than the size of the studied crystals. The high conductivity is also manifested via reduction of the quality factor of the spectrometer resonator from 3300 down to 2900 caused by insertion of the sample at 130 K. The variation of estimate of spins concentration with temperature could originate from thermal ionization of donors and increase of the sample conductivity. EPR signals with g-factor close to 1.96 in ZnO have been attributed to shallow donors in paramagnetic state[48-51].

For ZSb01_3, ZAs02_3 and ZSb02_1 samples two signals: with g-factors close to 1.955 and complex signal with g-factor between 2.001 and 2.012 have been observed. Concentration of paramagnetic centers with g-factor close to 1.955 have been estimated as $5.9 \cdot 10^{19}$ spin/g, $3.2 \cdot 10^{19}$ spin/g, $5.4 \cdot 10^{19}$ spin/g, respectively. For Sb and As doped samples signal with g-factor close to 1.955 is more symmetric than in pristine ZnO sample likely due to lower electrical conductivity of these samples. Indeed no reduction of the quality factor of the resonator caused by insertion of these samples was observed at 130 K. Estimates of paramagnetic centers concentrations with g-factor close to 2.005 are $1.8 \cdot 10^{17}$ spin/g, $3.1 \cdot 10^{18}$ spin/g, $2.1 \cdot 10^{17}$ spin/g for ZSb01_3, ZAs02_3 and ZSb02_1 samples, correspondingly. EPR signals with g-factor between 2.001 and 2.012 were previously attributed to zinc vacancies and their complexes[48-49]. Thus, EPR data points to the formation of zinc vacancies and their complexes in Sb- and As-doped ZnO. According to this interpretation doping of ZnO with As leads to more effective formation of zinc vacancies and their complexes than doping of ZnO with Sb at the same synthesis conditions. EPR data point to lower conductivity of doped samples compared to pristine ZnO. The decrease of conductivity could be

explained by compensation of shallow donors by zinc vacancies and their complexes acting as acceptors.

Addition of the group-V elements into the high-pressure cell qualitatively affects the growth of ZnO single crystals even when taken in low concentrations. Expectedly, the method yields much smaller crystals compared to undoped ZnO. The size drastically depends on both the nature and the concentration of the dopant. It appears that doping with phosphorus is generally difficult at high temperatures due to its chemical activity leading to formation of phosphates, which quickly cause the cessation of the crystal growth before any sizable crystals could be formed. Doping with As and Sb – typical semimetals from the same group – has a similar effect on the growth. An increase of concentration naturally causes a decrease of the size practically yielding a polycrystalline product at the upper limit of the studied range of concentrations (5% in our case). The best results were achieved for elemental As and Sb for which the size of individual crystals reaches 200 μm. Additionally, use of 3:2 stoichiometric mixtures of Zn and a group-V element designed to emulate the X^{-3} state does not create X^{-3} centers in ZnO according to XPS, but negatively affects the growth yielding significantly smaller crystals compared to other sources of dopants taken in the same concentrations.

While there is no direct way to prove that the group-V elements incorporate in the ZnO lattice, a complex of independent measurements practically provides an irrefutable evidence that incorporation indeed takes place. The main argument is EDX that not only detects the presence of the group-V elements but also allows to determine the actual concentration of a dopant in ZnO. Note, that a direct analytical approach is not applicable in this case as most of the dopant is solidified on the surface of crystals and not actually included in the lattice. The concentrations were consistently found to be ~0.3 at% when doping with As and Sb. Particularly valuable data was obtained in experiments where EDX spectra were recorded from a thin section from the middle part of a crystal. The concentrations were found to be ~0.2 at%, which is only very slightly lower than those from local parts of the surface. This value could be considered the thermodynamic solubility of As and Sb in ZnO at the synthetic conditions.

Another proof of dopant incorporation is XPS after Ar^{+} etching that reveals formation of X^{+3} centers. When substituting Zn in ZnO this impurities induce formation of V_{Zn} due to a large mismatch of ionic radii. The spectral methods including photoluminescence, EPR and Raman spectroscopy all prove that V_{Zn} and their complexes are formed as a result of doping. Moreover, EPR of As-doped ZnO contains a complex signal that corresponds not only to V_{Zn} but also to several V_{Zn}-complexes, one of which was determined as $(V_{Zn}^{-})_2$. A similar signal with g-factor between 2.001 and 2.012 was observed for ZSb01_3; however, its intensity was too low to reliably ascribe its components. Overall, it is highly likely that there are more V_{Zn}-based defect complexes that may or may not be associated with X^{+3} centers. This suggestion is also supported by the Raman study. The amount of V_{Zn} per one dopant atom estimated from Raman shift is significantly higher than 2 as one would expect for the simple $As(Sb)_{Zn}$-$2V_{Zn}$ acceptor complex. It implies a more

complicated nature of acceptor behavior of the group-V elements and its role in generation of V_{Zn} than formation of only $As(Sb)_{Zn}$-$2V_{Zn}$ complex.

4 Conclusions

The unique growth method of ZnO single crystals doped with the group-V elements from the melt at high pressure was proposed for the first time that allows direct introduction of the desired dopant in the structure due to its homogeneous distribution in the melt. Such doping causes distinct changes in size and morphology compared to undoped ZnO crystals grown from the melt. The level of doping was estimated from EDX data as 0.2-0.3 at%. Grown crystals exhibit shiny photoluminescence under UV excitation in the visible wavelength range that features a yellow band with the maximum at 565 nm, which as has been previously reported originates from V_{Zn}-associated acceptors. Estimates of V_{Zn} concentration from noticeable Raman shifts of A_1(TO) peak show that the number of V_{Zn} induced per one atom of dopant is significantly higher than 2 as in $As(Sb)_{Zn}$-$2V_{Zn}$ complex. The EPR study demonstrates that other V_{Zn}-complexes such as $(V_{Zn}^{-})_2$ are generated as well, which does not happen without doping. The present result proves that such doping indeed creates acceptor centers in ZnO single crystals and implies that the acceptor behavior of the group-V elements in ZnO may be not only due to formation of $As(Sb)_{Zn}$-$2V_{Zn}$ shallow acceptor but also other acceptor complexes.

Acknowledgements

The authors acknowledge support from Lomonosov Moscow State University Program of Development for providing access to the XPS and SEM facilities. Authors thank the MSU State Assignment (AAAA-A21-121011990019-4) and Dr. Konstantin I. Maslakov for XPS measurements. The work was supported by the RF President Grant for Leading Scientific Schools (Grant Number 2726.2020.3).

5 References

1 Wong, E. M.; Searson, P. C. ZnO Quantum Particle Thin Films Fabricated by Electrophoretic Deposition. *Appl. Phys. Lett.* **1999**, 74, 2939.

2 Yu, P.; Tang, Z. K.; Wong, G. K. L.; Kawasaki, M.; Ohtomo, A.; Koinuma, H.; Segawa, Y. Room-Temperature Gain Spectra and Lasing in Microcrystalline ZnO Thin Films. *J. Cryst. Growth.* **1998**, 184–185, 601–604.

3 Bagnall, D. M.; Chen, Y. F.; Zhu, Z.; Yao, T. Optically Pumped Lasing of ZnO at Room Temperature. *Appl. Phys. Lett.* **1997**, 70, 2230.

4 Choopun, S.; Vispute, R. D.; Noch, W.; Balsamo, A.; Sharma, R. P.; Venkatesan, T. Oxygen Pressure-tuned Epitaxy and Optoelectronic Properties of Laser-Deposited ZnO Films on Sapphire. *Appl. Phys. Lett.* **1999**, 75, 3947.

5 Ko, H. J.; Chen, Y. F.; Zhu, Z.; Yao, T. Photoluminescence Properties of ZnO Epilayers Grown on CaF_2 (111) by Plasma Assisted Molecular Beam Epitaxy. *Appl. Phys. Lett.* **2000**, 76, 1905.

6 Janotti, A.; Van de Walle, C. G. Native Point Defects in ZnO. *Phys. Rev. B.* **2007**, 76, 165202.

7 Zhang, S. B.; Wei, S.-H.; Zunger, A. Intrinsic n-Type versus p-Type Doping Asymmetry and the Defect Physics of ZnO. *Phys. Rev. B.* **2001**, 63, 075205.

8 Van de Walle C. G. Hydrogen as a Cause of Doping in Zinc Oxide. *Phys. Rev. Lett.* **2000**, 85, 1012.

9 Li, J.; Wei, S.-H.; Li, S.-S.; Xia, J.-B. Design of Shallow Acceptors in ZnO: First-Principles Band-Structure Calculations. *Phys. Rev. B.* **2006**, 74, 081201(R).

10 Puchala, B.; Morgan, D. Stable Interstitial Dopant-Vacancy Complexes in ZnO. *Phys. Rev. B.* **2012**, 85, 195207.

11 Avrutin, V.; Silversmith, D. J.; Morkoc, H. Doping Asymmetry Problem in ZnO: Current Status and Outlook. *Proc. IEEE.* **2010**, 98(7), 1269–1280.

12 Yan, Y.; Li, J.; Wei, S.-H.; Al-Jassim, M. M. Possible Approach to Overcome the Doping Asymmetry in Wideband Gap Semiconductors, *Phys. Rev. Lett.* **2007**, 98, 135506.

13 Limpijumnong, S.; Zhang, S. B.; Wei, S.-H.; Park, C. H. Doping by Large-Size-Mismatched Impurities: The Microscopic Origin of Arsenic- or Antimony-Doped p-Type Zinc Oxide, *Phys. Rev. Lett.* **2004**, 92, 155504.

14 Aoki, T.; Hatanaka, Y.; Look, D. C. ZnO Diode Fabricated by Excimer-Laser Doping. *Appl. Phys. Lett.* **2000**, 76, 3257.

15 Ryu, Y. R.; Zhu, S.; Look, D. C.; Wrobel, J. M.; Jeong, H. M.; White, H. W. Synthesis of p-Type ZnO Films. *J. Cryst. Growth.* **2000**, 216, 330–334.

16 Kim, K.-K.; Kim, H.-S.; Hwang, D.-K.; Lim, J.-H.; Park, S.-J. Realization of p-Type ZnO Thin Films via Phosphorus Doping and Thermal Activation of the Dopant. *Appl. Phys. Lett.* **2003**, 83, 63.

17 Huang, Y.-C.; Weng, L.-W.; Uen, W.-Y.; Lan, S.-M.; Li, Z.-Y.; Liao, S.-M.; Lin, T.-Y.; Yang, T.-N. Annealing Effects on the p-Type ZnO Films Fabricated on GaAs Substrate by Atmospheric Pressure Metal Organic Chemical Vapor Deposition. *J. Alloys Compd.* **2011**, 509(5), 1980–1983.

18 Yang, Z.; Chu, S.; Chen, W. V.; Li, L.; Kong, J.; Ren, J.; Yu, P. K. L.; Liu, J. ZnO:Sb/ZnO:Ga Light Emitting Diode on c-Plane Sapphire by Molecular Beam Epitaxy. *Appl. Phys. Express*. **2010**, 3, 032101.

19 Baranov, A. N.; Kovalenko, A. A.; Kononenko, O. V.; Emelin, E. V.; Matveev, D. V. Synthesis and Properties of Antimony-Doped ZnO Nanorods. *Inorg. Mater.* **2013**, 49(2) 127–135.

20 Triboulet, R. Scope of ZnO Growth. *Proc. SPIE*. **2001**, 4412, 1–8.

21 Grossner, U.; Christensen, J. S.; Svensson, B. G.; Kuznetsov, A. Yu. Carrier Concentration and Shallow Electron States in Sb-Doped Hydrothermally Grown ZnO. *Superlattices Microstruct.* **2007**, 42, 294–298.

22 Jang, S.; Chen, J.-J.; Kang, B. S.; Ren F.; Norton, D. P.; Pearton S. J.; Lopata J.; Hobson, W. S. Formation of p-n Homojunctions in n-ZnO Bulk Single Crystals by Diffusion From a Zn_3P_2 Source. *Appl. Phys. Lett.* **2005**, 87, 222113.

23 Taibarei, N. O.; Kytin, V. G.; Kupriyanov, E. E.; Kulbachinskii, V. A.; Makhiboroda, M. A.; Baranov, A. N. Creation of Acceptor Centers in ZnO Single Crystals by Annealing in Sb Vapor. *J. Phys. Chem. C*. **2019**, 123, 34, 20769–20773.

24 Jeong, T. S.; Han, M. S.; Youn, C. J. Raman Scattering and Photoluminescence of As Ion-Implanted ZnO Single Crystal. *J. Appl. Phys.* **2004**, 96, 175–179.

25 Zhang, S.; Yao, S.; Li, J.; Zhao, L.; Wang, J.; Boughton, R. I. Growth Habit Control of ZnO Single Crystals in Molten Hydrous Alkali Solutions. *J. Cryst. Growth.* **2011**, 336, 56–59.

26 Jacobs, K.; Schulz, D.; Klimm, D.; Ganschow, S. Melt Growth of ZnO Bulk Crystals in Ir Crucibles. *Solid State Sci*. **2010**, 12, 307–310.

27 Mukhanov, V. A.; Sokolov, P. S.; Baranov, A. N.; Timoshenko, V. Yu.; Zhigunov, D. M.; Solozhenko, V. L. Congruent Melting and Rapid Single-Crystal Growth of ZnO at 4 GPa. *CrystEngComm*. **2013**, 15, 6318–6322.

28 Baranov, A. N.; Sokolov, P. S.; Kurakevych, O. O.; Tafeenko, V. A.; Trots, D.; Solozhenko, V. L. Synthesis of Rock-Salt MeO–ZnO Solid Solutions (Me=Ni^{2+}, Co^{2+}, Fe^{2+}, Mn^{2+}) at High Pressure and High Temperature. *High Press. Res.* **2008**, 28, 515–519.

29 Mukhanov, V. A.; Sokolov, P. S.; Solozhenko, V. L. On Melting of B_4C Boron Carbide under Pressure. *J. Superhard. Mater*. **2012**, 34, 211–213.

30 Iwanaga, H.; Shibata, N.; Nittono, O.; Kasuga, M. Crystal Growth in *c* Direction and Crystallographic Polarity in ZnO Crystals. *J. Cryst. Growth.* **1978**, 45, 228–232.

31 Viltres, H.; Odio, O. F.; Lartundo-Rojas, L.; Reguera, E. Degradation Study of Arsenic Oxides under XPS Measurements. *Appl. Surf. Sci.* **2020**, 511, 145606.

32 Nolot, E.; Sabbione, C.; Pessoa, W.; Prazakova, L.; Navarro, G. Germanium, Antimony, Tellurium, Their Binary and Ternary Alloys and the Impact of Nitrogen: An X-ray Photoelectron Study. *Appl. Surf. Sci.* **2021**, 536, 147703.

33 Reshchikov, M. A.; Xie, J. Q.; Hertog, B.; Osinsky, A. Yellow Luminescence in ZnO Layers Grown on Sapphire. *J. Appl. Phys.* **2008**, 103, 103514.

34 Özgür, Ü.; Alivov, Ya. I.; Liu, C.; Teke, A.; Reshchikov, M. A.; Doğan, S.; Avrutin, V.; Cho, S.-J.; Morkoç, H. A Comprehensive Review of ZnO Materials and Devices. *J. Appl. Phys.* **2005**, 98, 041301.

35 Reshchikov, M. A.; Garbus, J.; Lopez, G.; Ruchala, M.; Nemeth, B.; Nause, *J. Mater. Res. Soc. Symp. Proc.* **2007**, 957, K07–19.

36 Chen, Y. N.; Xu, S. J.; Zheng, C. C.; Ning, J. Q.; Ling, F. C. C.; Anwand, W.; Brauer, G.; Skorupa, W. Nature of Red Luminescence Band in Research-Grade ZnO Single Crystals: A "Self-Activated" Configurational Transition. *Appl. Phys. Lett.* **2014**, 105, 041912.

37 Jindal, K.; Tomar, M.; Katiyar, R. S.; Gupta, V. Raman Scattering and Photoluminescence Investigations of N Doped ZnO Thin Films: Local Vibrational Modes and Induced Ferromagnetism. *J. Appl. Phys.* **2016**, 120, 135305.

38 Yang, B.; Feng, P.; Kumar, A.; Katiyar, R. S.; Achermann, M. Structural and Optical Properties of N-Doped ZnO Nanorod Arrays. *J. Phys. D: Appl. Phys.* **2009**, 42, 195402.

39 Fan, X. M.; Lian, J. S.; Zhao, L.; Liu, Y. H. Single Violet Luminescence Emitted from ZnO Films Obtained by Oxidation of Zn Film on Quartz Glass. *Appl. Surf. Sci.* **2005**, 252, 420–424.

40 Cuscó, R.; Alarcón-Lladó, E.; Ibáñez, J.; Artús, L.; Jiménez, J.; Wang, B.; Callahan, M. J. Temperature Dependence of Raman Scattering in ZnO. *Phys. Rev. B.* **2007**, 75, 165202.

41 Klingshirn, C. F.; Meyer, B. K.; Waag, A.; Hofmann, A.; Geurts, J. *Zinc Oxide. From Fundamental Properties towards Novel Applications*; Springer, 2010.

42 Ansel'm, A. I. *Introduction to Semiconductor Theory*; Prentice-Hall, 1981.

43 Chandraboss, V. L.; Karthikeyan, B.; Senthilvelan, S. Experimental and First-Principles Study of Guanine Adsorption on ZnO Clusters. *Phys. Chem. Chem. Phys.* **2014**, 16, 23461–23475.

44 Bond, W. L. Measurement of the Refractive Indices of Several Crystals, *J. Appl. Phys.* **1965**, 36, 1674–1677.

45 Vegesna, S. V.; Bhat, V. J.; Bürger, D.; Dellith, J.; Skorupa, I.; Schmidt, O. G.; Schmidt, H. Increased Static Dielectric Constant in ZnMnO and ZnCoO Thin Films with Bound Magnetic Polarons. *Sci. Rep*. **2020**, 10, 6698.

46 Samanta, K.; Arora, A. K.; Katiyar, R. S. Impurity Induced Bond-Softening and Defect States in ZnO:Cu. *J. Appl. Phys.* **2011**, 110, 043523.

47 Dyson, F. D. Electron Spin Resonance Absorption in Metals. II. Theory of Electron Diffusion and the Skin Effect. *Phys. Rev*. **1955**, 98, 349–359.

48 Durisic, A. B.; Choy, W. C. H.; Roy, V. A. L.; Leung, Yu. H.; Kwong, C. Y.; Cheah, K. W.; Rao, T. K. C.; Chan, W. K.; Lui, H. F.; Surya, C. Photoluminescence and Electron Paramagnetic Resonance of ZnO Tetrapod Structures. *Adv. Funct. Mater.* **2004**, 14, 856–864.

49 Stehr, J. E.; Johansen, K. M.; Bjørheim, T. S.; Vines, L.; Svensson, B. G.; Chen, W.; Buyanova, I. Zinc-Vacancy–Donor Complex: A Crucial Compensating Acceptor in ZnO. *Phys. Rev. Appl.* **2014**, 2, 021001.

50 Sann, J.; Stehr, J.; Hofstaetter, A.; Hofmann D. M.; Neumann, A.; Lerch, M.; Haboeck, U.; Hoffmann, A.; Thomsen, C. Zn Interstitial Related Donors in Ammonia-Treated ZnO Powders. *Phys. Rev. B.* **2007**, 76, 195203.

51 Vorobyeva, N.; Rumyantseva, M.; Filatova, D.; Konstantinova, E.; Grishina, D.; Abakumov, A.; Turner, S.; Gaskov A. Nanocrystalline ZnO(Ga): Paramagnetic Centers, Surface Acidity and Gas Sensor Properties. *Sens. Actuators B Chem*. **2013**, 182, 555–564.

Table 1. *List of the samples with the results of microscopy and XRD analysis.*

Sample name	**Composition, mol%**	**Description**	**Impurity phases**
ZSb02_1	ZnO + 2% Sb_2O_3	A blend of dark spherical (<50 μm) and rod-like crystals (up to 300 μm) with visible precipitation on the surface.	Sb
ZSb05_1	ZnO + 5% Sb_2O_3	Aggregated orange crystals, probably polycrystalline	Sb + Sb_2O_3
ZSb01_2	ZnO + 1% Zn_3Sb_2	Gray-white crystals with hexagonal faceting (d=20-80 μm),	Pure ZnO
ZSb02_2	ZnO + 2% Zn_3Sb_2	Aggregated colorless crystals d=20-60 μm	Sb + ZnSb
ZSb05_2	ZnO + 5% Zn_3Sb_2	Small aggregated gray-white crystals (d=5-20 μm)	Sb + ZnSb
ZSb01_3	ZnO + 1% Sb	Dark crystals, d=40-150 μm	Sb
ZP01_2	ZnO + 1% Zn_3P_2	Small (<20 μm) dark-gray crystals with drop-like inclusions on the surface; polycrystalline	Pure ZnO
ZP02_2	ZnO + 2% Zn_3P_2	Small polycrystalline dark-orange aggregates	Zn
ZP05_2	ZnO + 5% Zn_3P_2	Small polycrystalline dark-orange aggregates	Zn+$Zn_3(PO_4)_2$
ZP01_3	ZnO + 1% P	Small polycrystalline yellow aggregates	Pure ZnO
ZAs02_2	ZnO + 2% Zn_3As_2	Small dark crystals d=10-50 μm	As_2O_3
ZAs02_3	ZnO + 2% As	Dark crystals; d=50-200 μm	As+As_2O_3

Table 2. *Paramagnetic defects concentrations.*

Sample	**Type 1 defects concentration (g≈1.957), 10^{19} spin/g**	**Type 2 defects concentration (g≈2.002), 10^{18} spin/g**
Undoped ZnO	5.5 (4.6 at 180 K)	<0.05
ZSb01_3	5.9	0.18
ZAs02_3	3.2	3.1
ZSb02_1	5.4	0.21
ZSb01_2	1.5	<0.05

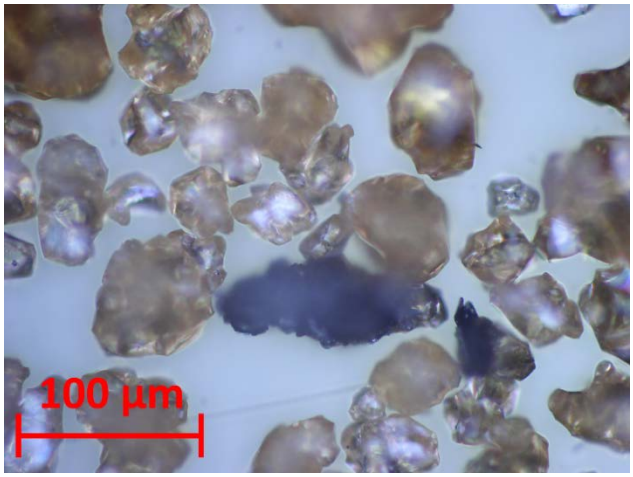

(a)

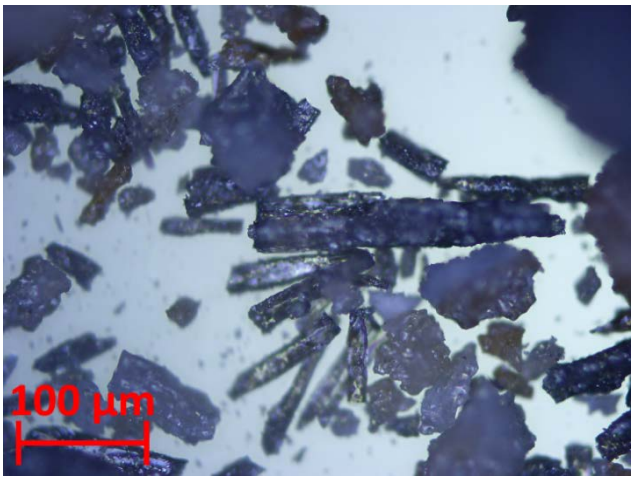

(b)

Figure 1 *Optical microscope images of ZSb01_1 (a) and ZSb02_1 (b) doped with 1 and 2 at% Sb_2O_3, respectively*

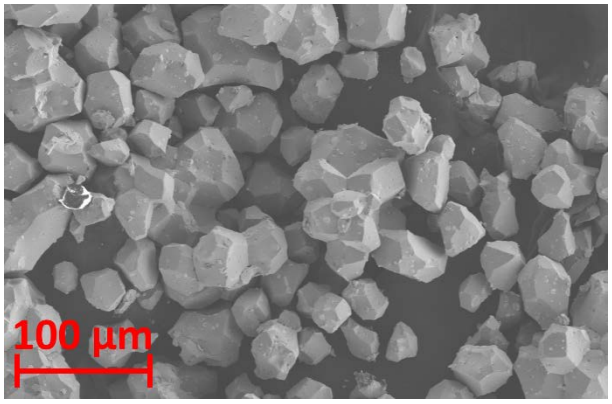

(a)

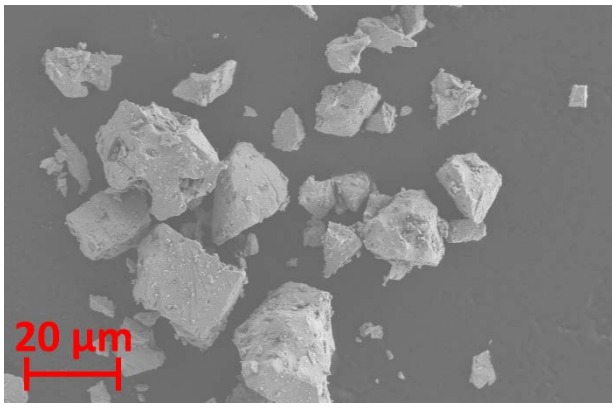

(b)

Figure 2 *SEM images of ZSb01_2 (a) and ZP01_2 (b) doped with 1% Zn_3Sb_2 and 1% Zn_3P_2, respectively.*

(a)

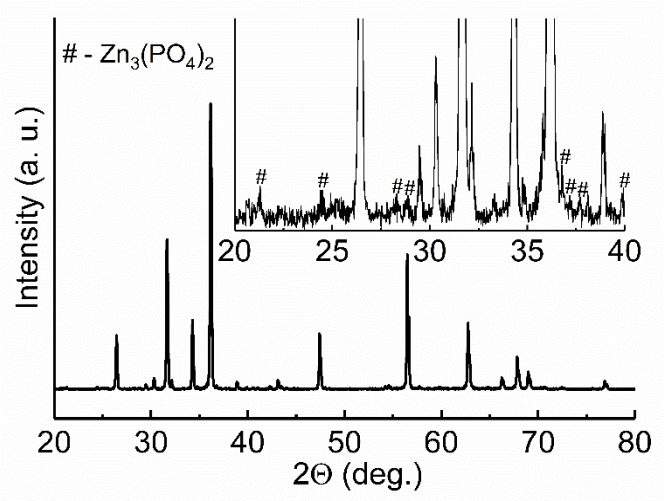

(b)

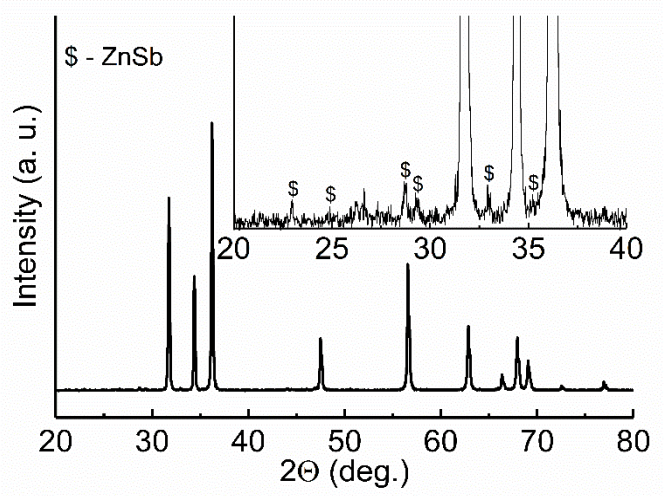

Figure 3 *Powder XRD patterns of ZP02_2 (a) and ZSb02_2 (b). The insets display the patterns with ×40 magnification.*

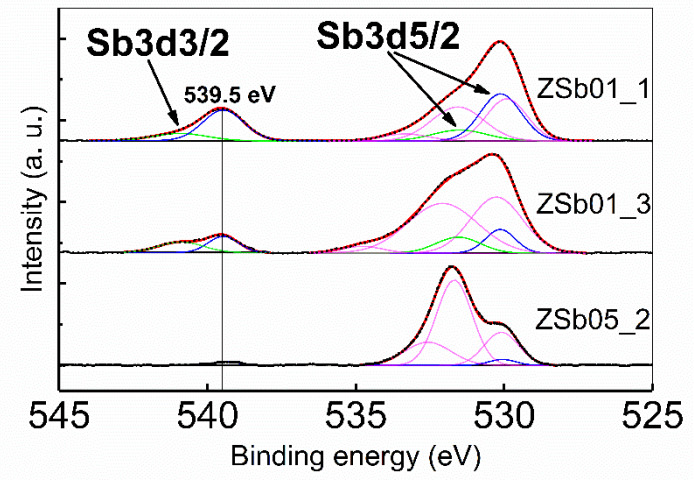

(a)

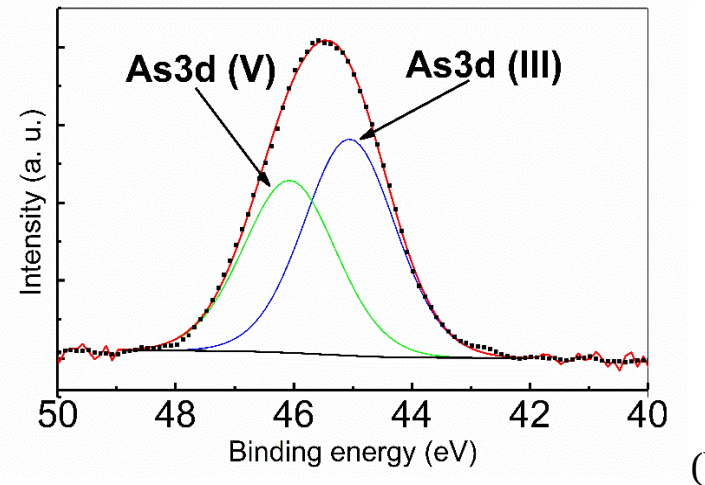

(b)

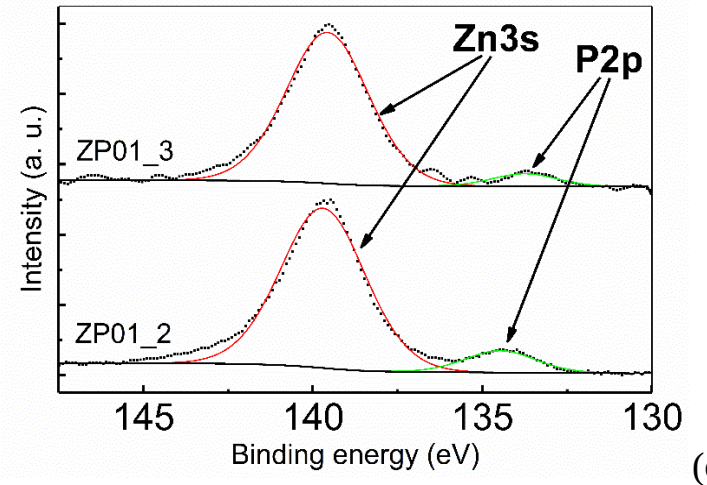

(c)

Figure 4. *XPS spectra of as-recovered discs. a – spectra of ZSb01_1, ZSb01_3, ZSb05_2, b – ZAs02_2, c – ZP01_3, ZP01_2. Blue and green lines correspond to +3 and +5 states of dopants, respectively. Purple lines correspond to O1s states. Red lines are integral fits of deconvoluted spectra. Black dotes represent experimental data.*

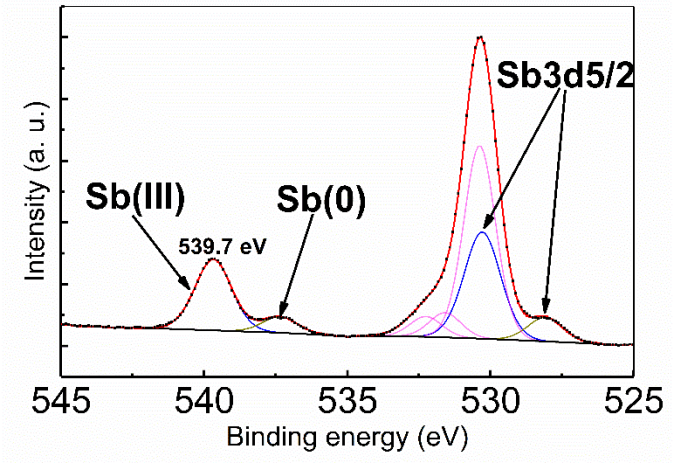

(a)

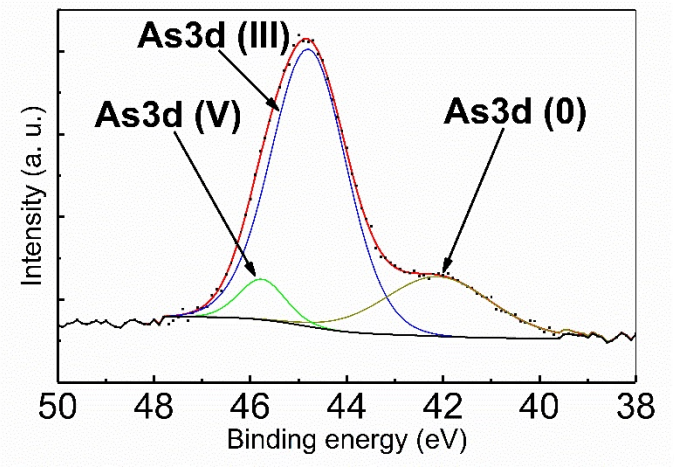

(b)

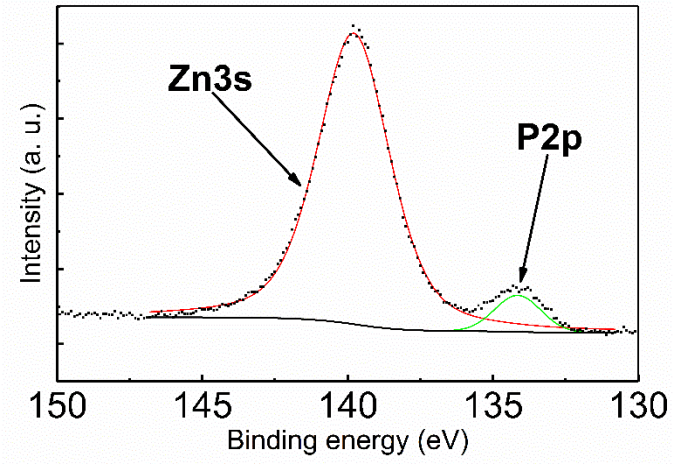

(c)

Figure 5 *XPS spectra after Ar^+ etching. a – ZSb01_1, b – ZAs02_2, c – ZP01_3. Blue and green lines correspond to +3 and +5 states of dopants, respectively. Dark yellow lines correspond to 0 oxidation state. Purple lines correspond to various O1s oxygen states. Red lines are integral fits of deconvoluted spectra. Black dots represent experimental data.*

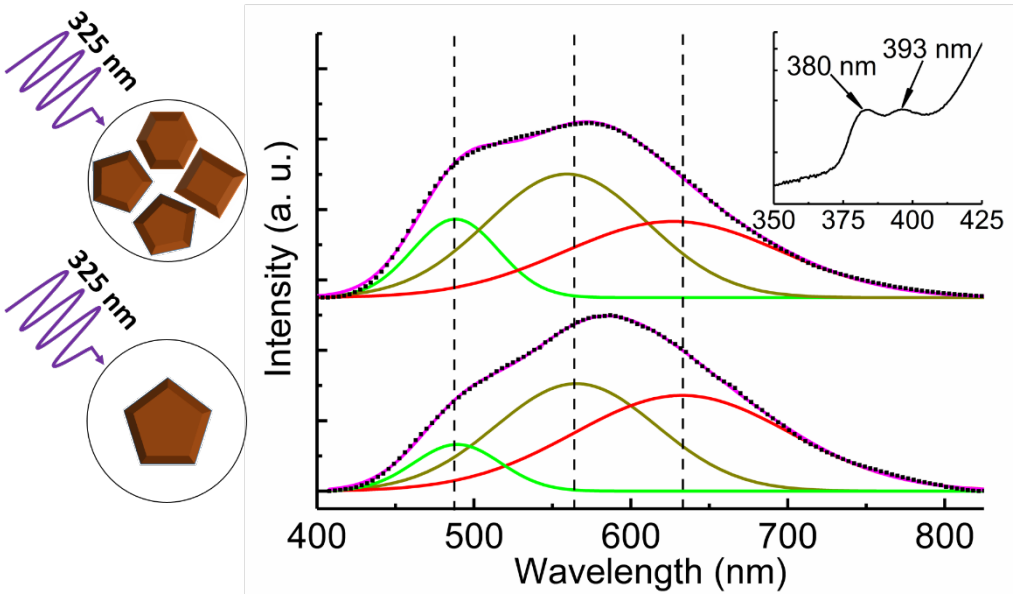

Figure 6 *Room-temperature PL spectrum of ZSb02_1. Black symbols are experimental data (every fifteenth point is shown); solid curves – fit of GL, YL and RL (with respective colors) components of defect luminescence band. The upper spectrum shows luminescence from a collective of randomly selected crystals. The lower spectrum shows luminescence from one single crystal. The inset shows NBE luminescence in semi-log coordinates of the same sample recorded independently.*

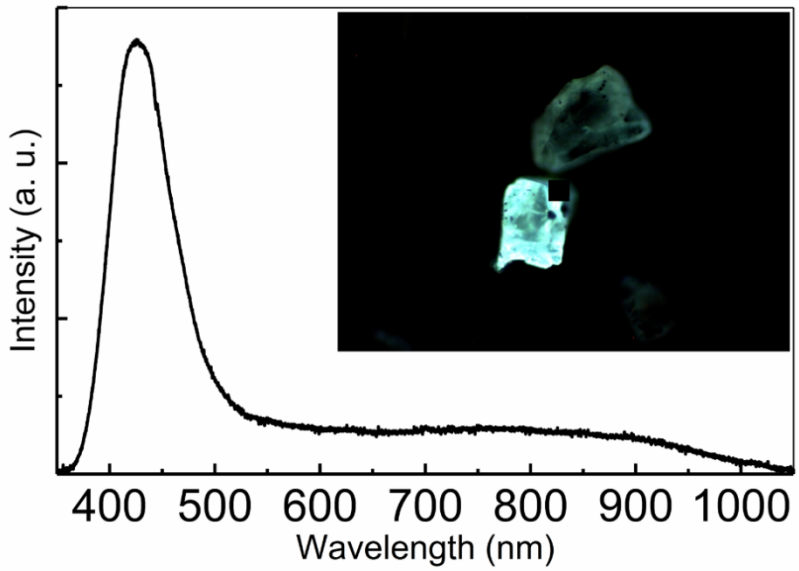

Figure 7 *Room-temperature PL spectrum of ZSb02_2. The inset shows microluminescence of individual crystals.*

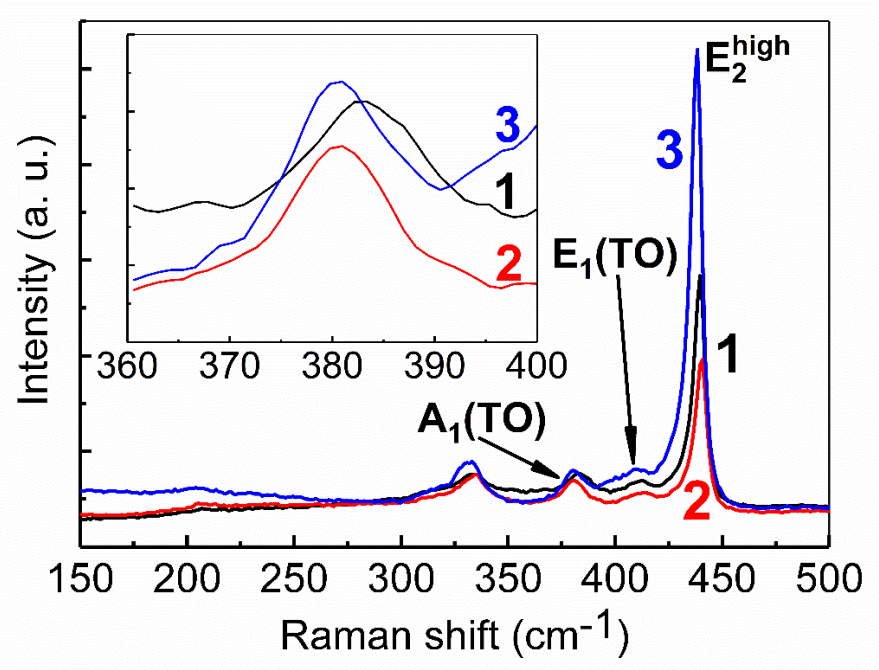

Figure 8 *Room-temperature Raman spectra of undoped ZnO single crystal (1), ZSb01_3 (2), and ZAs02_3 (3) samples. The inset shows A_1(TO) peak.*

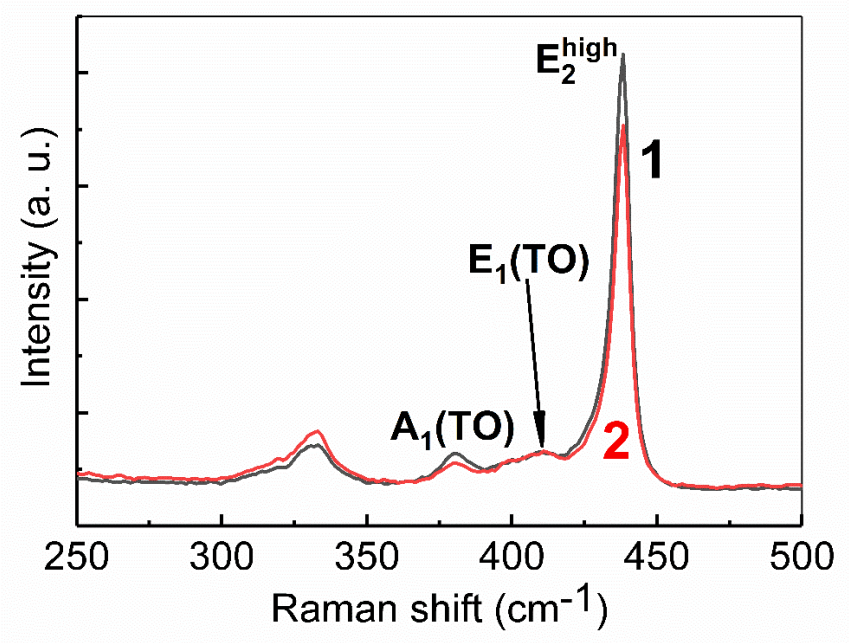

Figure 9 *Raman spectra of ZAs02_3 obtained with the analyzer for two directions of polarization of the exciting light, differing by 30º.*

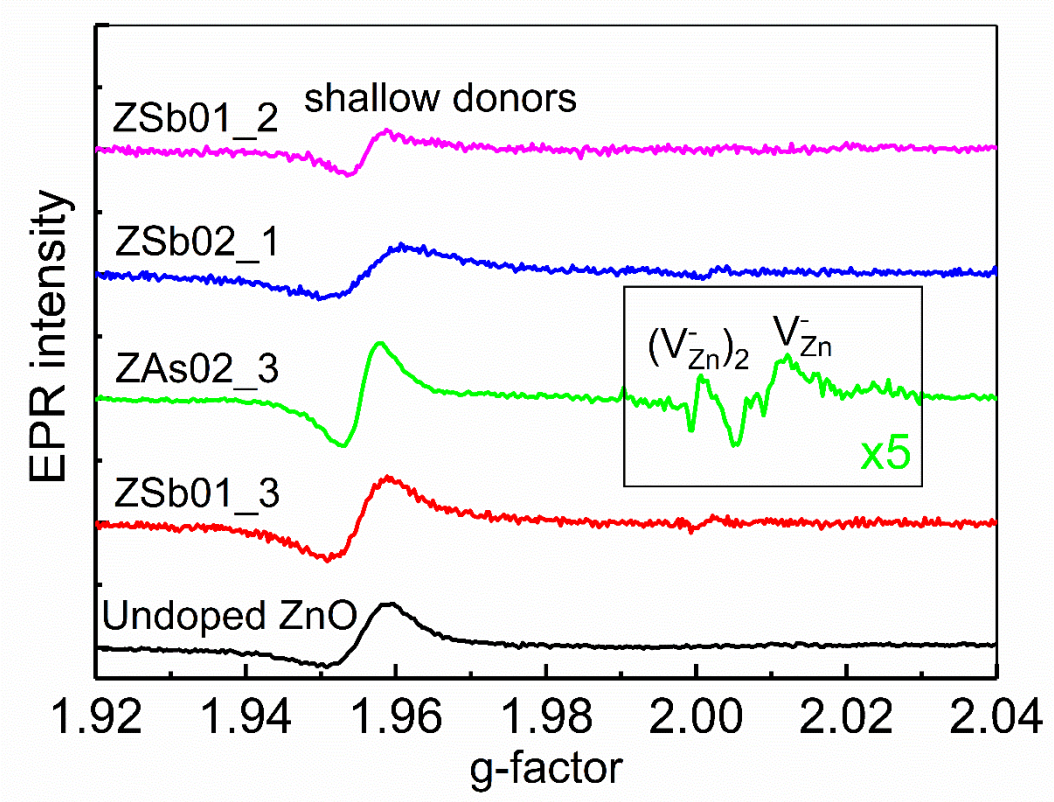

Figure 10 *EPR spectra of ZSb01_2, ZSb02_1, ZAs02_3, ZSb01_3 and undoped ZnO single crystal recorded at 130 K.*